Supporting Information

Interfacial hydrogen bond modulation of dynamic catalysts for nitrate electroreduction to ammonia

Yuchi Wan,[a] Yixiang Tang,[a] Yinze Zuo,[*a] Kaian Sun,[a] Zewen Zhuang,[a] Yun Zheng,[a] Wei Yan,[a] Jiujun Zhang[*a] and Ruitao Lv[*b]

[a] Institute of New Energy Materials and Engineering, Fujian Engineering Research Center of High Energy Batteries and New Energy Equipment & Systems, School of Materials Science and Engineering, Fuzhou University, Fuzhou, 350108, China

[b] State Key Laboratory of New Ceramics and Fine Processing, School of Materials Science and Engineering, Tsinghua University, Beijing, 100084, China

[*] Corresponding authors.

E-mail address: jiujun.zhang@fzu.edu.cn (Jiujun Zhang), lvruitao@tsinghua.edu.cn (Ruitao Lv).

Experimental Methods

Preparation of the Cr doped CoO_x electrocatalysts

The Cr doped CoO_x (Cr-CoO_x) electrocatalysts were synthesized by the ion exchange of ZIF-67 and subsequent calcination process. In details, a piece of Ni foam (1×3 cm^2) was firstly sonicated in a HCl solution (25 vol.%) for 15 minutes to remove the surface oxides, and then washed by ultrapure water. 30 mL 0.4 M 2-Methylimidazole aqueous solution was added into 30 mL 0.05 M $Co(NO_3)_2\cdot 6H_2O$ aqueous solution to form a mixed solution, then the pretreated Ni foam was inmersed into ththis mixed solution for 15 hours to obtain the sample of ZIF-67 supported on Ni foam (ZIF-67@NF). During the ion exchange process, the ZIF-67@NF was inmersed into 6 mM $Na_2CrO_4\cdot 4H_2O$ solutions for 2.5 hours to obtain the Cr doped ZIF-67@NF (Cr-ZIF-67@NF). Finally, this Cr-ZIF-67@NF was clacinated at 500 °C for 1 hour under the mixed Ar/H_2 atmosphere to synthesize the Cr doped CoO_x electrocatalyst loaded on Ni foam.

Preparation of the control samples

The Mo doped CoO_x (Mo-CoO_x) electrocatalyst loaded on Ni foam was also prepared by a similar method by replacing $Na_2CrO_4\cdot 4H_2O$ solution with $Na_2MoO_4\cdot 2H_2O$ solution with the same concentration. The W doped CoO_x (W-CoO_x) electrocatalyst loaded on Ni foam was prepared by a similar method by replacing $Na_2CrO_4\cdot 4H_2O$ solution with $Na_2WO_4\cdot 2H_2O$ solution with the same concentration. The CoO_x electrocatalyst loaded on Ni foam was prepared by direct calcination of ZIF-67@NF without ion exchange process.

Characterizations

X-ray diffraction (XRD) patterns were collected by a Bruker D8 Advance using Cu Kα radiation (40 kV, 40 mA). Scanning electron microscope (SEM) images were obtained by a field emission scanning electron microscope (Verios G4), which was equipped with an energy

dispersive spectroscopy (EDS) detector. Transmission electron microscope (TEM) images were obtained by a FEI Tecnai F20 with a field emission gun operating at 200 kV, and elemental-mapping information was obtained by the corresponding EDS. X-ray photoelectron spectroscopy (XPS) spectra were collected on a Thermo Scientific K-Alpha, and the obtained XPS data were calibrated by shifting the C 1s peaks to 284.8 eV. Raman data were collected on the Witec Alpha 300R Raman system using the excitation wavelength of 532 nm. The absorbance data of the spectrophotometer were collected on the UV7600 ultraviolet-visible (UV-vis) spectrophotometer.

Electrochemical nitrate reduction tests

All electrochemical tests were conducted by the CHI760E electrochemical workstation. Electrocatalytic nitrate reduction experiments were carried out on a H-type cell equipped with an anion exchange membrane (FAB-PK-130). In the three-electrode configuration, the as-prepared self-supported material was directly used as the working electrode, the Hg/HgO electrode was used as the reference electrode, and Pt foil was used as the counter electrode. All potentials were referenced against the reversible hydrogen electrode (RHE) based on the Nernst equation ($E_{RHE} = E_{Hg/HgO} + 0.059 \times pH + 0.098$). Before electrochemical tests, the electrolyte was saturated by Ar gas to remove the dissolved O_2 and the electrolyte was stirred at 500 rpm. Linear sweep voltammogram (LSV) tests were performed from +0.4 V to –0.8 V vs. RHE at a scan rate of 5 mV s^{-1}. For electrocatalytic ammonia synthesis experiments, potentiostatic tests were performed at different potentials ranging from –0.1 V to –0.7 V vs. RHE for 1 hour, and the electrolyte was collected to analyze the liquid products.

Ammonia quantification

The ammonia concentration was determined by the indophenol blue method. In details, 2 mL diluted electrolyte was mixed with 2 mL NaOH solution (1 M, containing 5 wt.% salicylic acid and 5 wt.% sodium citrate), 1 mL NaClO (0.05 M) and 0.2 mL $C_5FeN_6Na_2O$ aqueous solution (1 wt.%). After this solution standed in darkness for 2 hours, the absorption spectrum was measured using a UV-vis spectrophotometer. The formation of indophenol blue was determined using absorbance at a wavelength of 655 nm. The concentration-absorbance curves were calibrated using standard solutions with a series of ammonia concentrations. The standard curve was plotted with the absorbance values at a wavelength of 655 nm on the *y-axis* and the concentration of NH_3 on the *x-axis*. The obtained standard curve (y=0.04686+0.48277x, R^2=0.999) showed a good linear relation of absorbance value with NH_3 concentration.

Determination of hydrazine

The hydrazine (N_2H_4) concentration was measured by the Watt and Chrisp method. The color reagent was prepared by dissolving 0.998 g p-Dimethylaminobenzaldehyde in the mixture of 5 mL concentrated HCl and 50 mL ethanol. 3 mL above prepared color reagent was mixed with 3 mL electrolyte and then standing in darkness for 10 minutes. The absorbance of N_2H_4 in the resulting electrolyte was estimated at 460 nm. Absolute calibration was achieved using hydrazine hydrate solutions of known concentrations as the standards, and the fitting curve showed a good linear relation of absorbance with N_2H_4·concentration (y=0.06766+1.11523x, R^2=0.999).

Determination of NO_3^-

In a typical procedure, 5.0 mL of standard or diluted sample solutions were mixed with 0.10 mL of 1.0 M HCl and 0.01 mL of 0.8 wt.% sulfamic acid solution. After shaking up and standing for 5 min, the NO_3^- concentration was measured using a UV-vis spectrophotometer at a

wavelength range from 210 nm to 300 nm. The NO_3^- concentration was estimated by the absorbance at 220 nm and 275 nm. Absolute calibration was achieved using $NaNO_3$ solutions of known concentrations as the standards, and the fitting curve showed a good linear relation of the calculated absorbance ($A=A_{220nm}-2A_{275nm}$) with NO_3^-·concentration ($y=0.05735+0.0527x$, $R^2=0.999$).

***Determination of* NO_2^-**

The NO_2^- concentration was measured by the Griess reaction. Firstly, the NO_2^- color reagent was prepared by dissolving 0.2g N-(1-Naphthyl) ethylenediamine dihydrochloride and 4 g sulfanilamide in the mixture of 10 mL phosphoric acid and 90 mL ultrapure water. Then 0.10 mL of color reagent was added to 5.0 mL of standard or diluted sample solutions, and standing for 20 minutes. The NO_2^- concentration was measured using a UV-vis spectrophotometer at wavelength range from 450 nm to 650 nm. The absorbance of NO_2^- in the resulting electrolyte was estimated at 540 nm. Absolute calibration was achieved using $NaNO_2$ solutions of known concentrations as the standards, and the fitting curve showed a good linear relation of absorbance with NO_2^-·concentration ($y=0.05645+0.20322x$, $R^2=0.999$).

^{15}N isotopic labeling measurement

The ^{15}N isotopic labeling experiment was carried out using $K^{15}NO_3$ (Aladdin, 99 atom%) as the ^{15}N source. After electrochemical nitrate reduction for 1 hour at –0.4 V vs. RHE in 1 M KOH containing 0.1 M $^{15}NO_3^-$, the produced $^{15}NH_3$ was determined by ^1H nuclear magnetic resonance (^1H NMR, Bruker 600MHz). In details, the pH of the diluted electrolyte was firstly adjusted to 2~3, and then 425 μL of electrolyte was mixed with 50 μL DMSO-d6 and 25 μL maleic acid (5000 ppm) as an internal standard for ^1H NMR measurement.

In-situ electrochemical XRD measurements

In-situ electrochemical XRD measurements were conducted on a customized PEEK cell (EC-XRD, Beijing Scistar Technology Co., Ltd) with a kapton membrane window, and the electrolyte was flowed by the peristaltic pump. To avoid the influence of Ni foam, the electrocatalyst was loaded on the carbon cloth support serving as the working electrode. The Pt wire was used as the counter electrode and a Hg/HgO electrode was used as the reference electrode. The pattern was collected in the 2θ range from 30° to 90° under an applied potential from 0 V to −0.7 V vs. RHE.

In-situ electrochemical Raman spectroscopy measurements

In-situ electrochemical Raman spectroscopy measurements were conducted on the Witec Alpha 300R Raman system, and the data were collected at 5 s exposure time averaged over 20 scans. Potentiostatic tests were performed at different potentials ranging from 0 V to −0.7 V vs. RHE in a customized Teflon cell (EC-Raman-H, Beijing Scistar Technology Co., Ltd) with a quartz window, and the electrolyte was flowed by the peristaltic pump. The self-supported material as the working electrode was immersed in electrolyte, and the electrode plane was kept perpendicular to the laser. The Raman spectroscopy at each applied potential was recorded after 1 minute of potentiostatic test.

In-situ electrochemical ATR-FTIR measurements

In-situ electrochemical ATR-FTIR was performed on the Thermo Scientific Nicolet iS50 spectrometer equipped with a liquid N_2-cooled MCT-A detector. The self-supported material as the working electrode was press against the silicon crystal covered by a gold film, forming a thin electrolyte layer between the working electrode and the silicon crystal. Potentiostatic tests were performed at different potentials ranging from +0.3 V to −0.7 V vs. RHE in a customized Teflon cell (EC-ATR-H, Beijing Scistar Technology Co., Ltd), and the electrolyte was flowed

by the peristaltic pump. Background spectrum was taken at the open-circuit potential. FTIR spectra at each applied potential were recorded after 1 minute of potentiostatic test. The spectra were obtained from an average of 32 scans with a resolution of 4 cm^{-1}.

Calculations of NH_3 yield rate and Faradaic efficiency

The NH_3 yield rate (R) was determined using the following equation:

$$R = \frac{C \cdot V}{t \cdot S} \tag{S1}$$

where C is the measured NH_3 concentration, V is the volume of the electrolyte, t is the reaction time, and S is the geometric area of the electrocatalyst.

The Faradaic efficiency (η) was determined using the following equation:

$$\eta = \frac{n \cdot F \cdot C \cdot V}{M \cdot Q} \tag{S2}$$

where n is the number of electrons required for producing one NH_3 molecule (n=8), F is the Faraday constant (F= 96485.33), C is the measured NH_3 concentration, V is the volume of the electrolyte, M is the relative molecular mass of NH_3 (M=17), and the Q is the total charge passed through the electrodes.

The NH_3 partial current density (j) was determined using the following equation:

$$j = \frac{Q \cdot FE}{t \cdot m} \tag{S3}$$

where Q is the total charge passed through the electrodes, FE is the Faradaic efficiency, t is the reaction time, and m is the geometrical area of the working electrode.

Theoretical calculations

Molecular Dynamic (MD) calculations were conducted by the Forcite module in Materials Studio comprising 145 H_2O molecules, 2 KOH and 1 KNO_3 molecules. All the size and dimensions of the simulation box is about 16.7 Å. The COMPASS II force field was used within

the simulation system. First, the geometry optimization algorithm was used with a combination of steepest descent, adopting basis Newton-Raphson, and quasi-Newton methods based on the convergence of the total energy (0.0001 kcal mol^{-1}) with a force of 0.05 kcal mol^{-1} $Å^{-1}$. After geometric optimization, an NPT (10 ps) pre-equilibrium simulation with constant particle numbers, pressure and temperature was initiated under a pressure of 0.1 MPa, a constant temperature of 298 K, and the Berendsen barostat was used to control the Andersen thermostat Pressure. Then, a 10 ps equilibrated NVT (constant number of particles, volume, and temperature) simulation was conducted under a pressure of 0.1 MPa, using the Nosé-Hoover thermostat to sustain the system at 298 K. Forcite analysis was used to calculate the MD results. The number of hydrogen bond is analyzed by the MD trajectory using TCL script in VMD. A hydrogen bond is defined when the O–O distance is shorter than 3.5 Å and the O–O–H angle is less than 35°.

The binding energies was conducted by Density Functional Theory (DFT) in the Vienna Ab Initio Simulation Package by applying Generalized Gradient Approximation (GGA) with the Perdew, Burke, and Ernzerhof (PBE) exchange-correlation functional and the Local Density Approximation (LDA). The all-electron Projector Augmented Wave (PAW) method implemented by Kresse and Joubert was also utilized. In details, as for Co slab, four atomic layers of the Co (001) slab with the supercell of 2 × 2. The $Co(OH)_2$ are used to construct the 2 × 1 $Co(OH)_2$ (001) slab. The Cr-$Co(OH)_2$ slab was obtained by replacing a fraction of Co of $Co(OH)_2$ by Cr.The kinetic energy cutoff for all the computations was set 450 eV, which was accompanied with a total energy convergence set at 10^{-5} eV for self-consistent iterations. The atomic forces fell below 0.02 eV/Å was applied for geometry optimization with a 2 × 2 × 1 Gamma k-point grid. An over 15 Å thick vacuum layer was performed to simulate surfaces and interfaces. In calculations, the treatment of long-range weak van der Waals interactions was

enhanced by incorporating the DFT-D3 method. The adsorption energy ($E_{ads.}$) was calculated according to the following equation:

$E_{ads.} = E_{adsorbate+surface} — E_{adsorbate} — E_{surface}$

where $E_{adsorbate+surface}$ is the total energy of the surface with the adsorbate, and $E_{adsorbate}$ and $E_{surface}$ are the energies of the free adsorbate molecule and the clean surface, respectively. A negative E_{ads} value represents an exothermic adsorption, and a more negative value corresponds to a stronger adsorption.

The Gibbs free energy is calculated as follows:

$$G = E_{ads} + E_{ZPE} - TS + \int CpdT$$

where E_{ZPE} is the difference corresponding to the zero point energy between the adsorbed molecule and molecule in the gas phase, and S and $\int CpdT$ are one molecule entropy and enthalpy between adsorbed state and gas phase.

The transition state (TS) structures and reaction pathways were located using the climbing image nudged elastic band (CI − NEB) method. The minimum energy path was optimized using a force-based conjugate-gradient method until the maximum force was below 0.05 eV/Å. In this work, stable adsorbed species were set as the initial state (IS) and finial state (FS) in the search for the TS. The barrier (Ea) and reaction energy (H) were estimated as $E_{TS} – E_{IS}$ and $E_{FS} – E_{IS}$, respectively.

Supplementary Figures

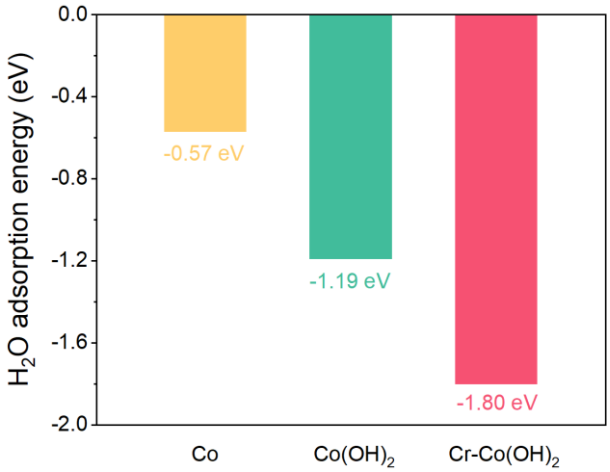

Figure S1. Comparison of H_2O adsorption energy of Cr-$Co(OH)_2$, $Co(OH)_2$, and Co.

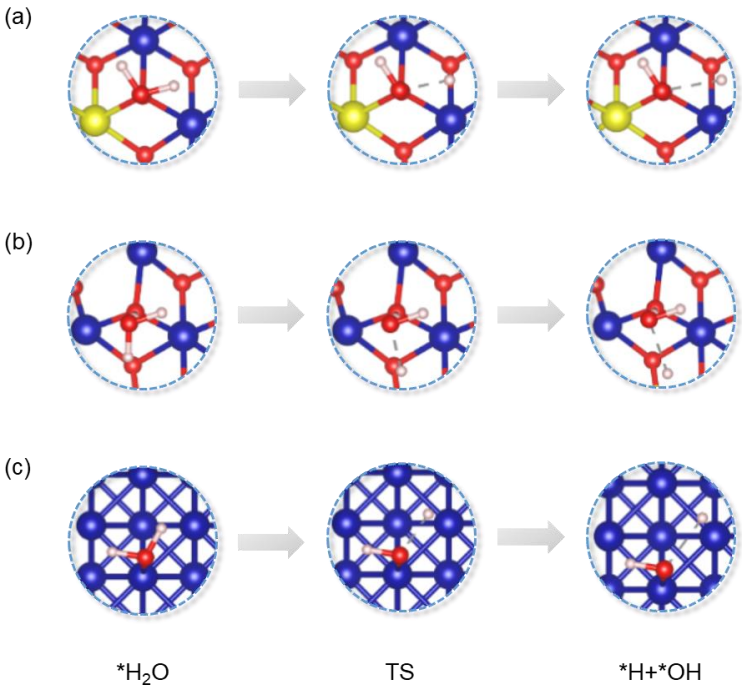

Figure S2. H_2O dissociation processes of (a) Cr-$Co(OH)_2$, (b) $Co(OH)_2$, and (c) Co.

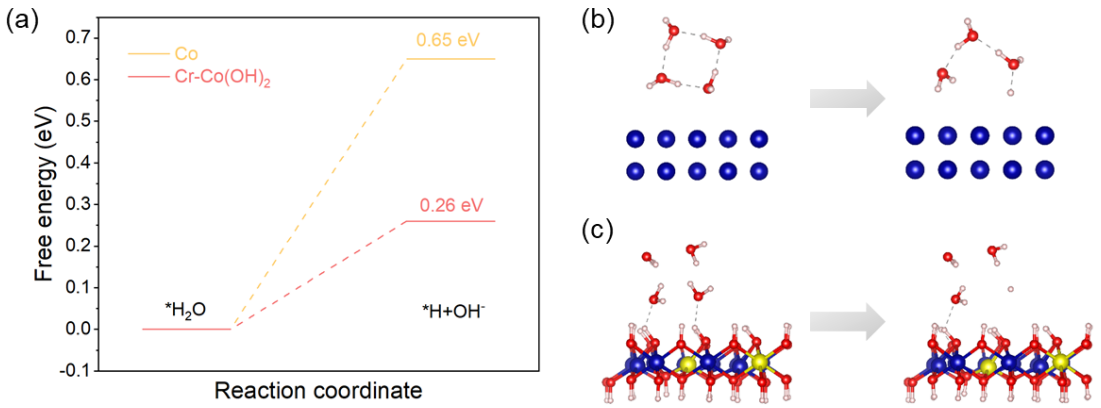

Figure S3. (a) Free energy of the *H formation from the dissociation of adsorbed H_2O in the solvated environment for Cr-$Co(OH)_2$ and Co. (b) Change of adsorption structure of solvated H_2O molecules on Co during the dissociation of adsorbed H_2O. (c) Change of adsorption structure of solvated H_2O molecules on Cr-$Co(OH)_2$ during the dissociation of adsorbed H_2O.

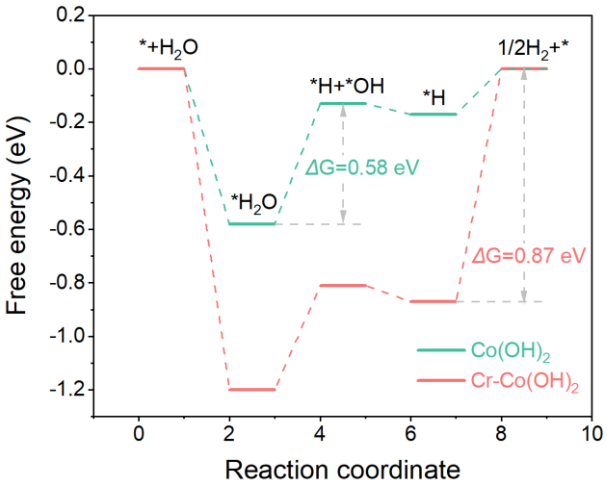

Figure S4. Free energy diagrams of HER on Cr-$Co(OH)_2$ and $Co(OH)_2$ electrocatalysts.

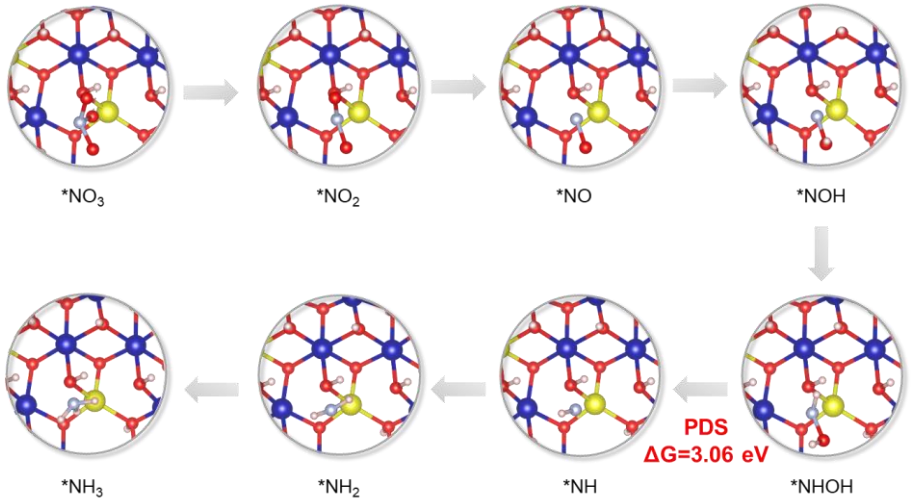

Figure S5. Adsorption structures of each intermediate on Cr-Co(OH)$_2$.

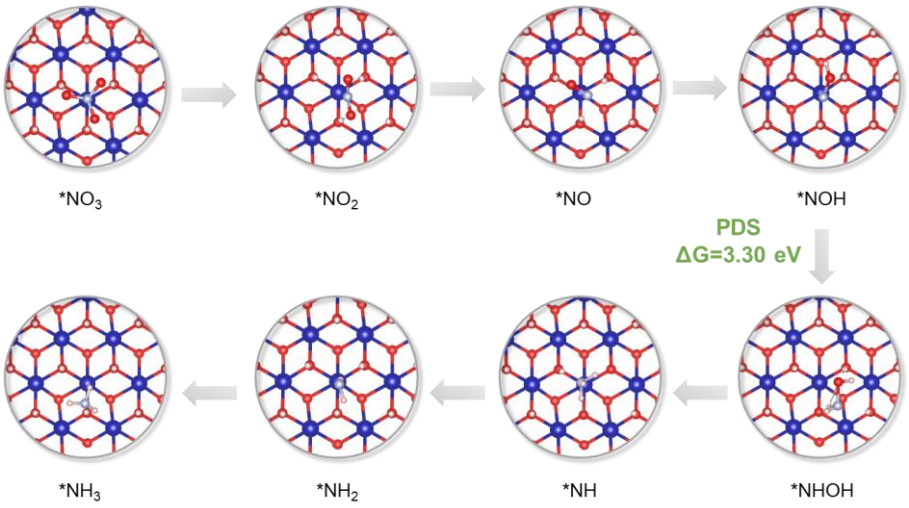

Figure S6. Adsorption structures of each intermediate on $Co(OH)_2$.

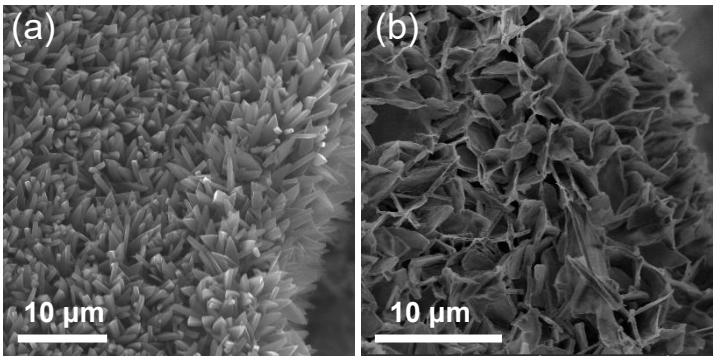

Figure S7. SEM images of (a) ZIF-67, and (b) Cr doped ZIF-67.

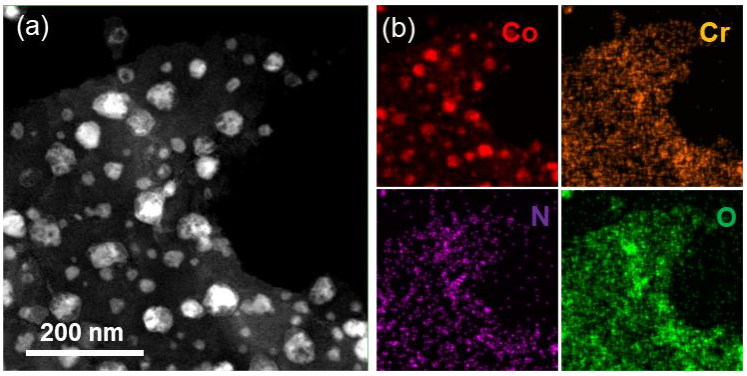

Figure S8. (a) HAADF STEM and (b) corresponding EDS elemental mapping images of the Cr-CoO_x electrocatalyst.

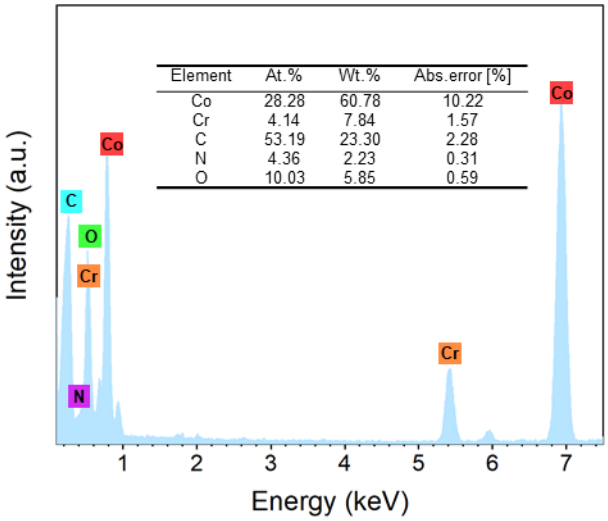

Figure S9. EDS elemental analysis of the Cr-CoO_x electrocatalyst.

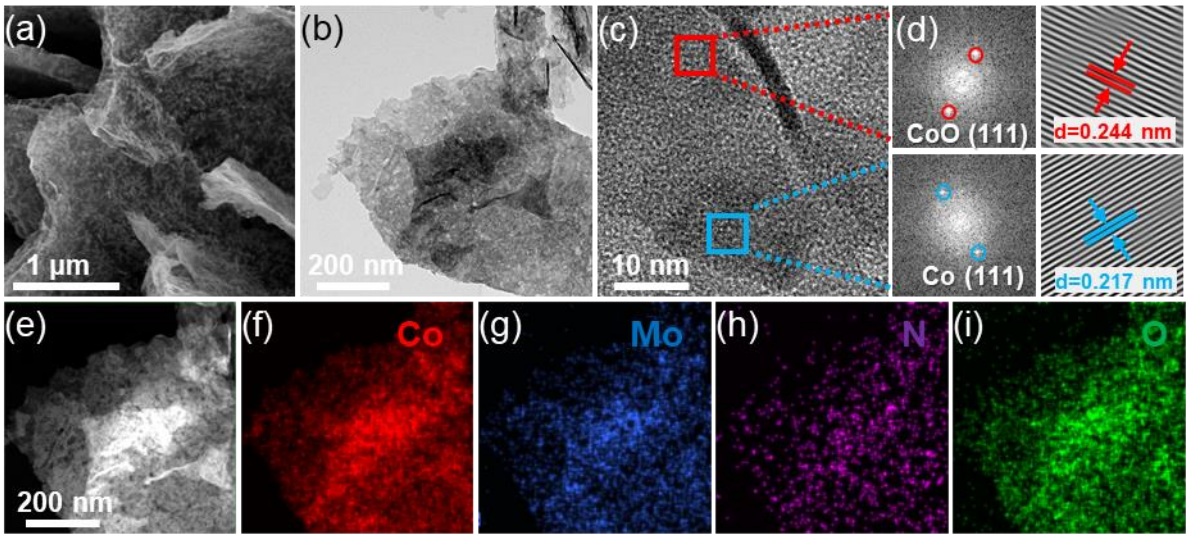

Figure S10. Morphology and structure characterizations of the Mo-CoO_x electrocatalyst. (a) SEM, (b) TEM, (c) HRTEM and d) corresponding FFT and IFFT images. (e-i) HAADF-STEM and corresponding EDS elemental mapping images.

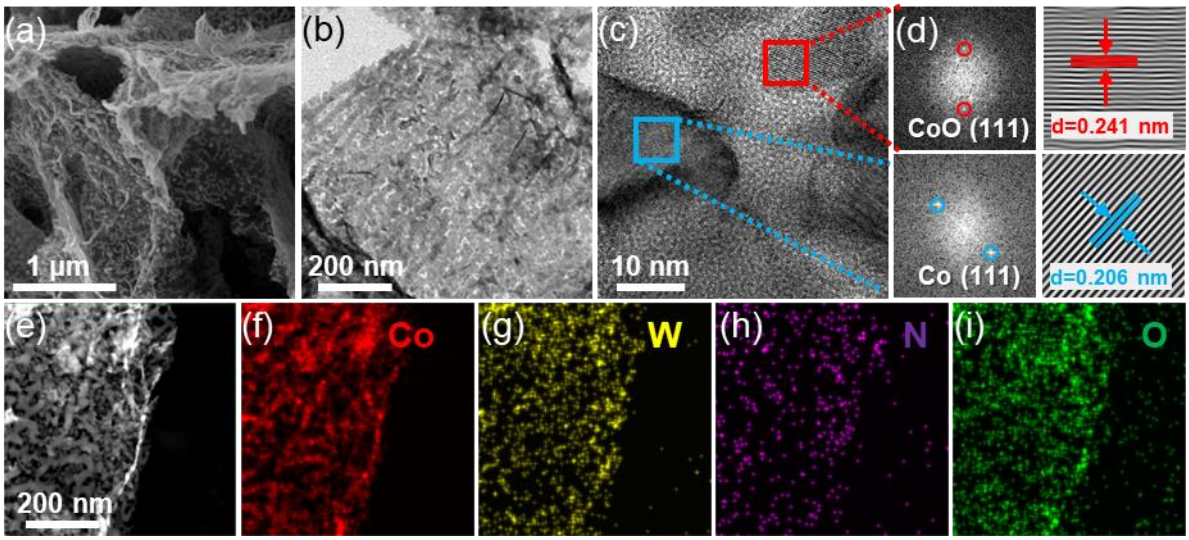

Figure S11. Morphology and structure characterizations of the W-CoO_x electrocatalyst. (a) SEM, (b) TEM, (c) HRTEM and d) corresponding FFT and IFFT images. (e-i) HAADF-STEM and corresponding EDS elemental mapping images.

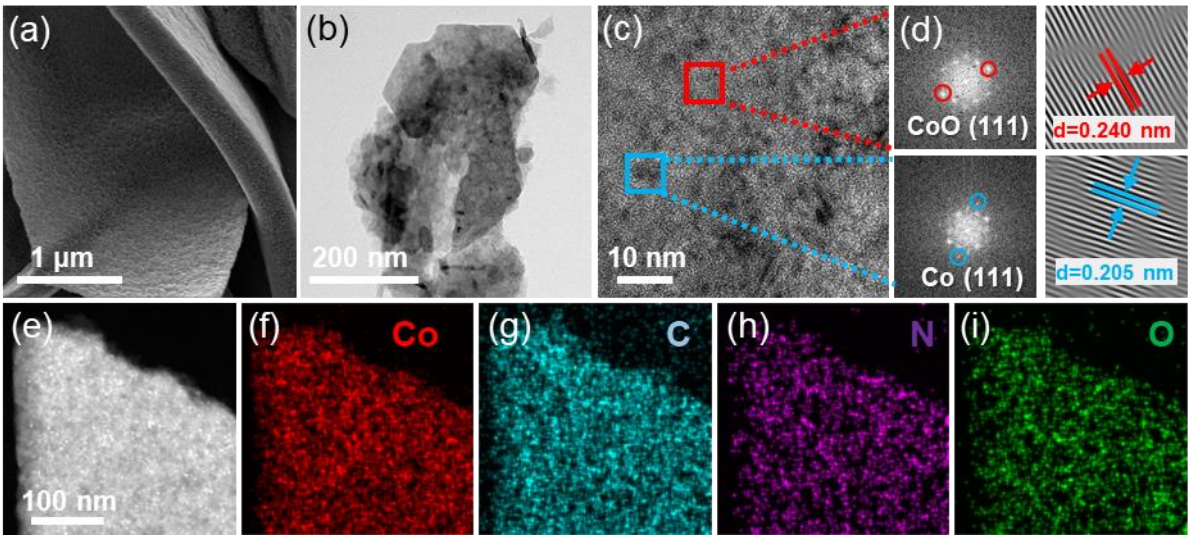

Figure S12. Morphology and structure characterizations of the CoO_x electrocatalyst. (a) SEM, (b) TEM, (c) HRTEM and d) corresponding FFT and IFFT images. (e-i) HAADF-STEM and corresponding EDS elemental mapping images.

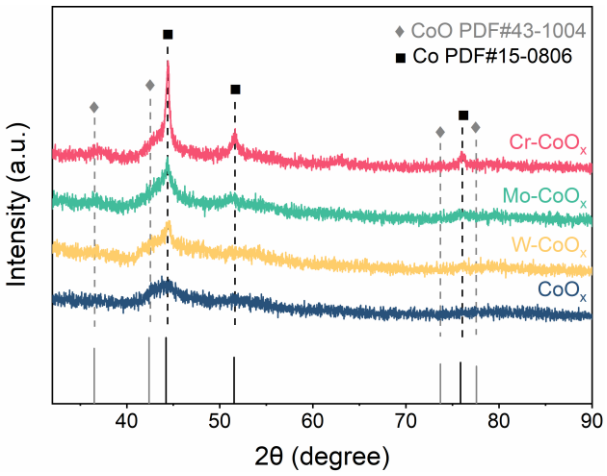

Figure S13. XRD patterns of different electrocatalysts.

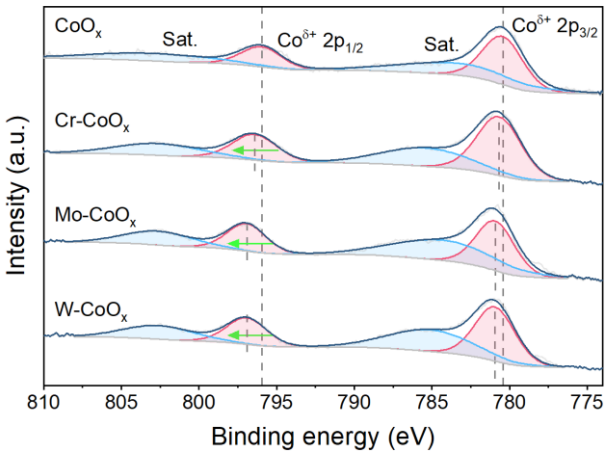

Figure S14. Co 2p XPS fine scan spectra of different prepared samples.

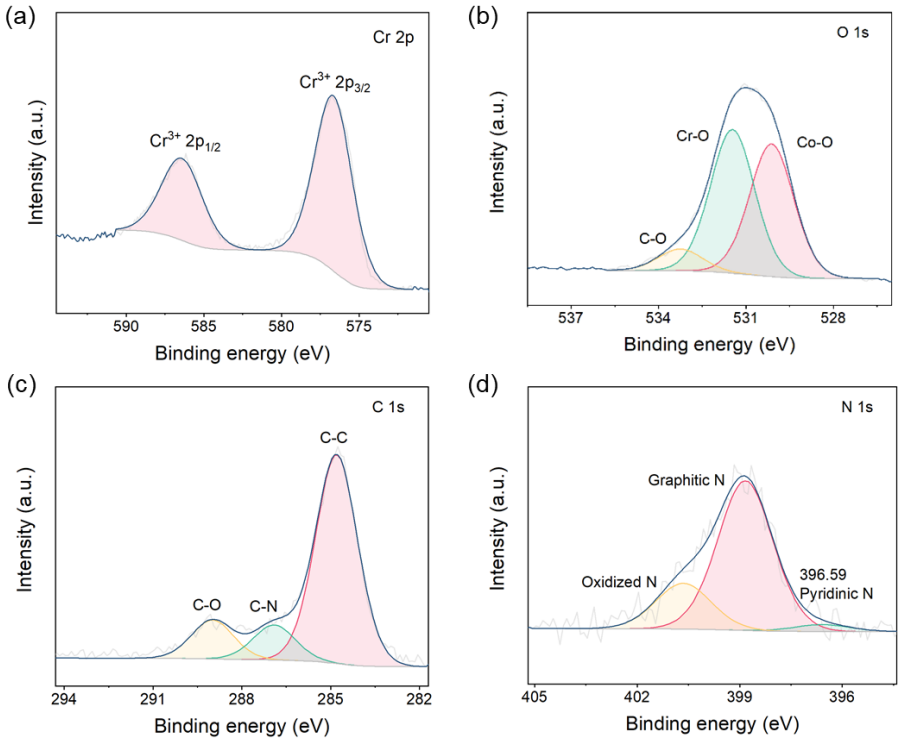

Figure S15. High resolution XPS spectra of (a) Cr 2p, (b) O 1s, (c) C 1s, and (d) N 1s of the Cr-CoO_x.

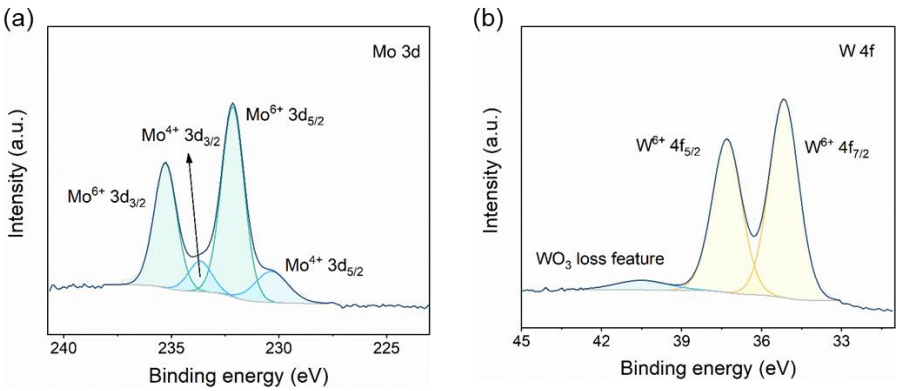

Figure S16. (a) Mo 3d XPS fine scan spectra of the Mo-CoO_x. (b) W 4f XPS fine scan spectra of the W-CoO_x.

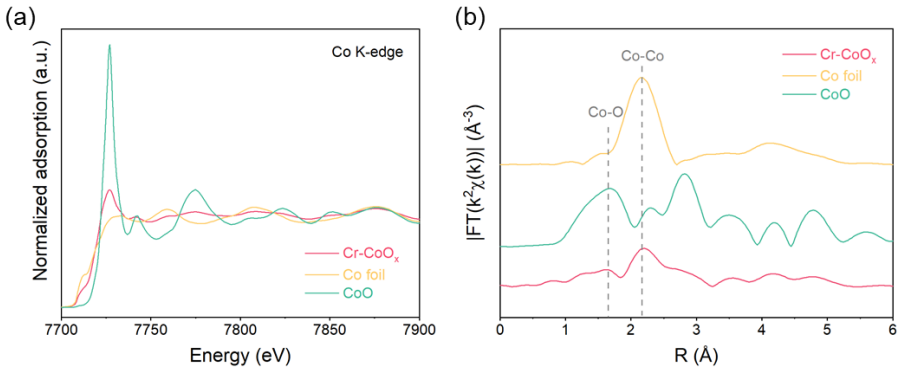

Figure S17. (a) Co K-edge XANES spectra, and (b) EXAFS spectra of the Cr-CoO_x and reference samples.

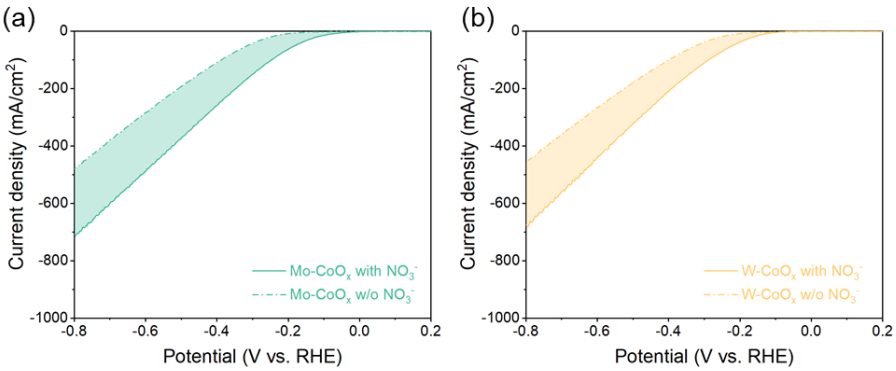

Figure S18. LSV curves without iR compensation for the (a) Mo-CoO_x, and (b) W-CoO_x in 1 M KOH with and without 0.1 M NO_3^-.

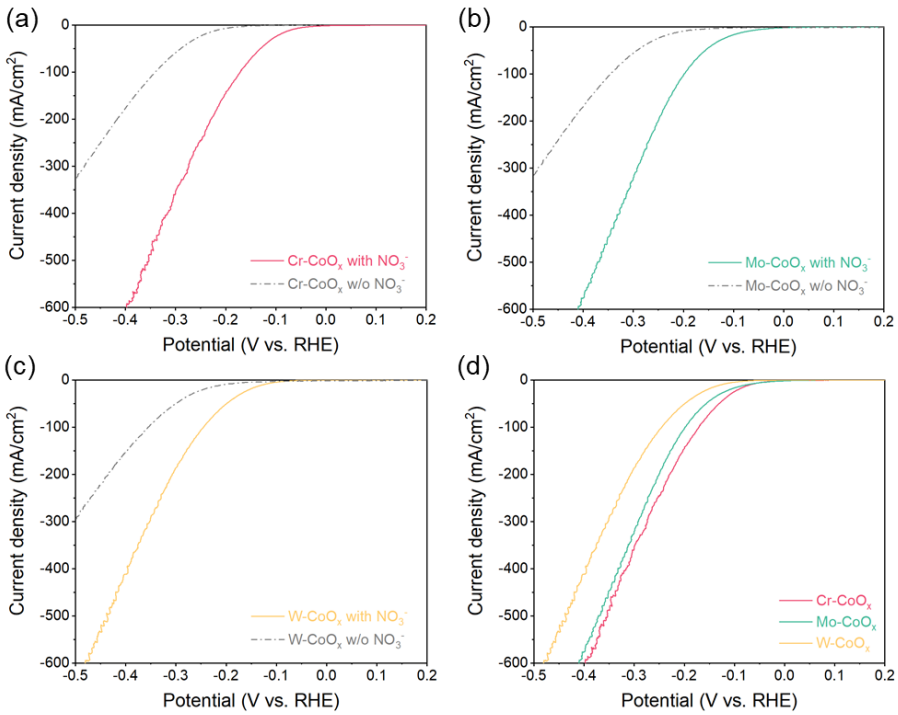

Figure S19. LSV curves with 50% iR compensation for the (a) Cr-CoO_x, (b) Mo-CoO_x, (c) W-CoO_x in 1 M KOH with and without 0.1 M NO_3^-. (d) Comparison of LSV curves with 50% iR compensation of different electrocatalysts with 0.1 M NO_3^-.

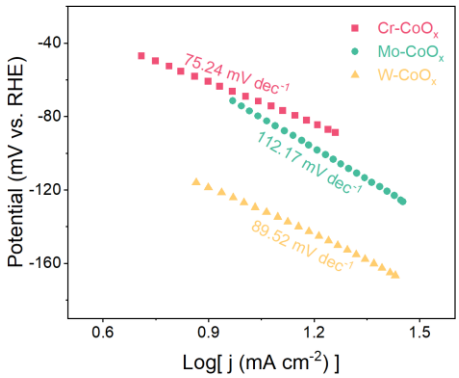

Figure S20. Tafel plots of the Cr-CoO_x, Mo-CoO_x, and W-CoO_x in 1 M KOH with 0.1 M NO_3^-.

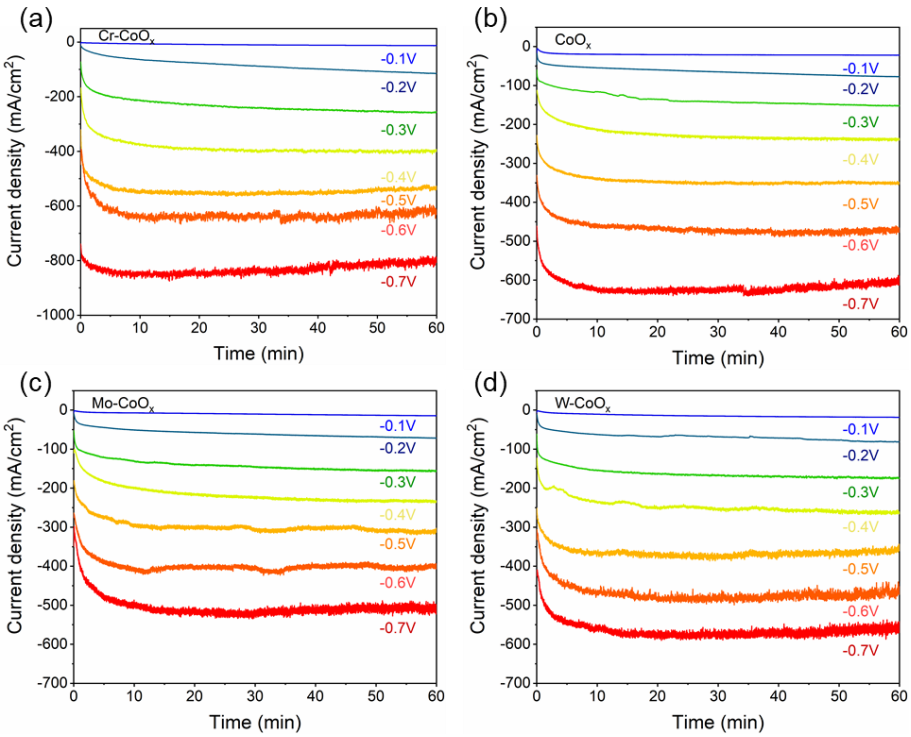

Figure S21. Chronoamperometric curves of the (a) Cr-CoO_x, (b) CoO_x, (c) Mo-CoO_x and (d) W-CoO_x.

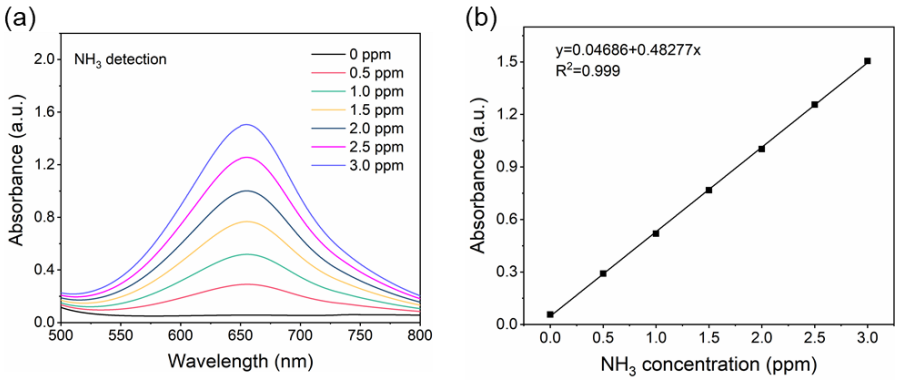

Figure S22. Calibrations with NH_3 standard solutions. (a) Spectrophotometric UV-vis curves and (b) calibration curve used for the quantification of NH_3 concentration. The absorbance at 655 nm was measured by a UV-vis spectrophotometer, and the fitting curve shows good linear relation of absorbance with NH_3 concentration ($y=0.04686+0.48277x$, $R^2=0.999$).

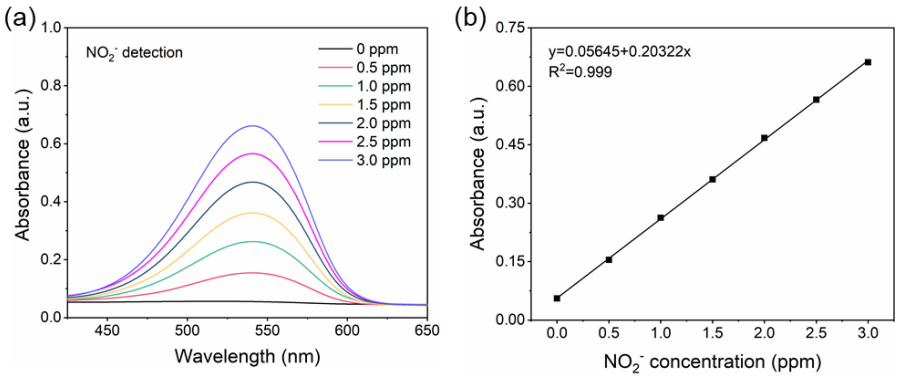

Figure S23. Calibrations with NO_2^- standard solutions. (a) Spectrophotometric UV-vis curves and (b) calibration curve used for the quantification of NO_2^- concentration. The absorbance at 550 nm was measured by a UV-vis spectrophotometer, and the fitting curve shows good linear relation of absorbance with NO_2^- concentration (y=0.05645+0.20322x, R^2=0.999).

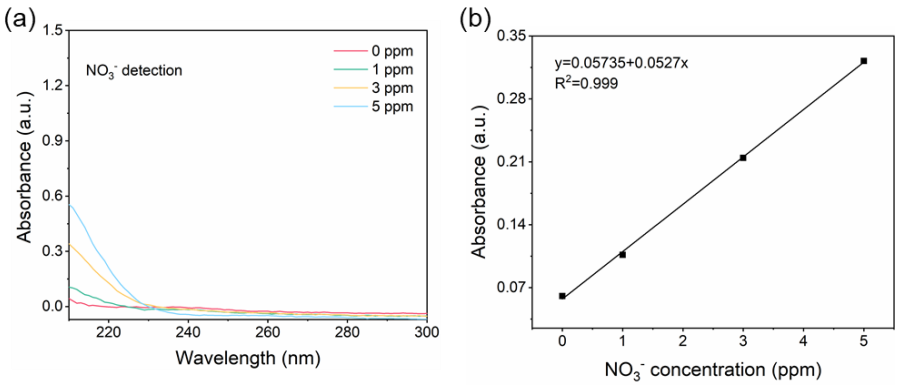

Figure S24. Calibrations with NO_3^- standard solutions. (a) Spectrophotometric UV-vis curves and (b) calibration curve used for the quantification of NO_3^- concentration. The absorbance at 220 nm and 275 nm were measured by a UV-vis spectrophotometer, and the fitting curve shows good linear relation of absorbance ($A=A_{220nm}-A_{275nm}$) with NO_3^- concentration ($y=0.05735+0.0527x$, $R^2=0.999$).

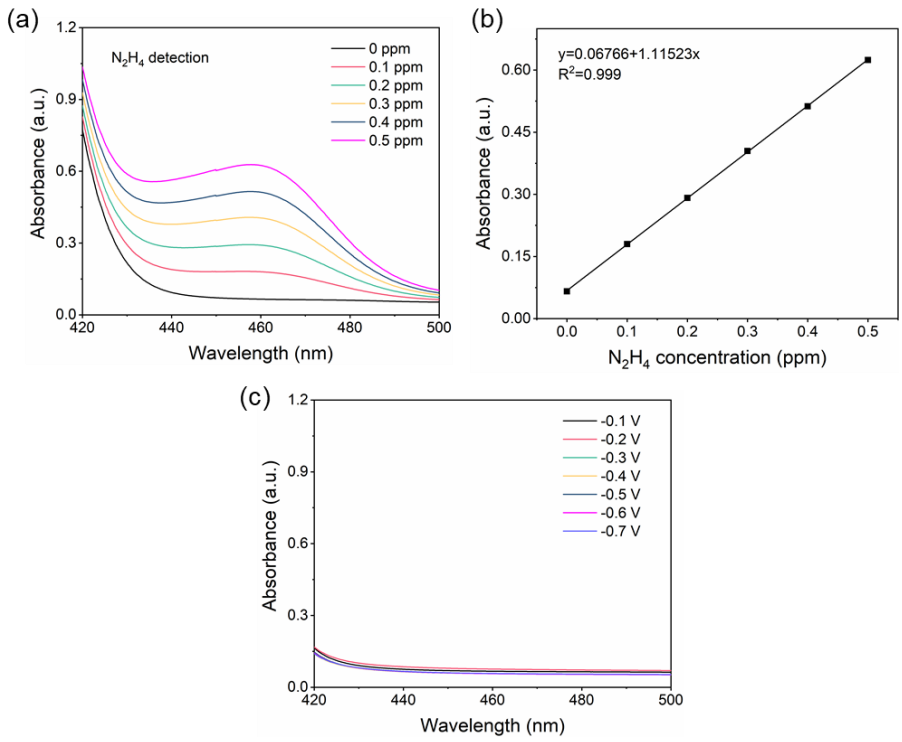

Figure S25. Calibrations with N_2H_4 standard solutions. (a) Spectrophotometric UV-vis curves and (b) calibration curve used for the quantification of N_2H_4 concentration. The absorbance at 460 nm were measured by a UV-vis spectrophotometer, and the fitting curve shows good linear relation of absorbance with N_2H_4 concentration (y=0.06766+1.11523x, R^2=0.999). (c) UV-vis absorption spectra of the electrolytes stained with N_2H_4 color indicator after electrocatalytic NO_3^-RR on the Cr-CoO_x electrocatalyst at different potentials. The UV-vis absorption spectra show weak signals for N_2H_4, confirming the absence of N_2H_4 byproduct during the electrochemical NH_3 synthesis.

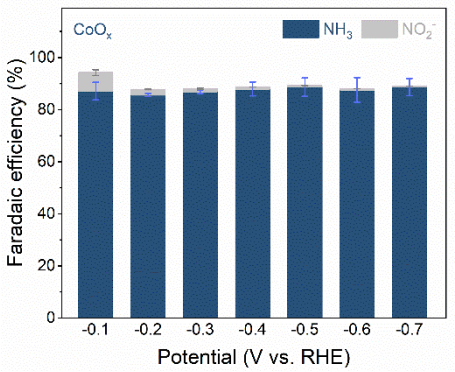

Figure S26. Faradaic efficiency of NH_3 and NO_2^- for the CoO_x electrocatalyst at different potentials.

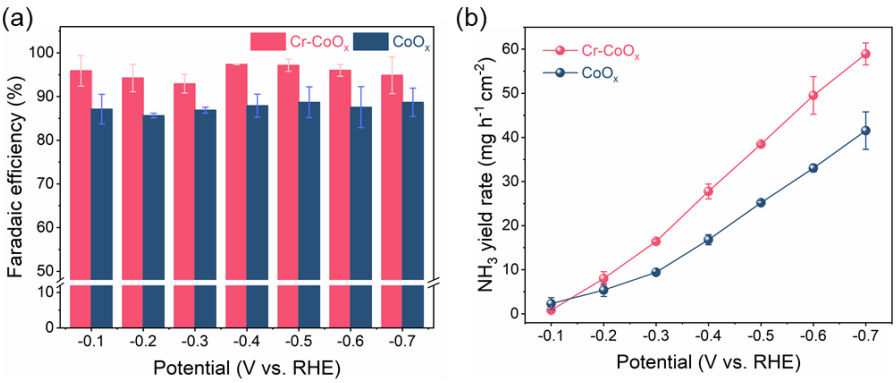

Figure S27. (a) Faradaic efficiency of NH_3 and (b) NH_3 yield rate comparison of the Cr-CoO_x and CoO_x.

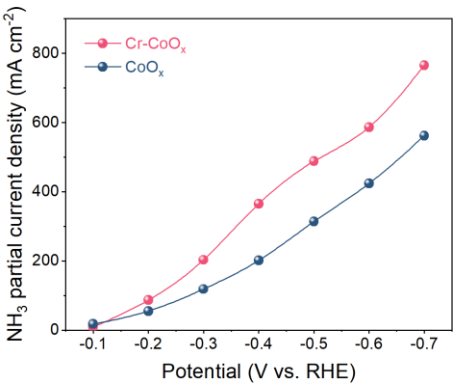

Figure S28. NH_3 partial current density for the Cr-CoO_x and CoO_x electrocatalysts at different potentials.

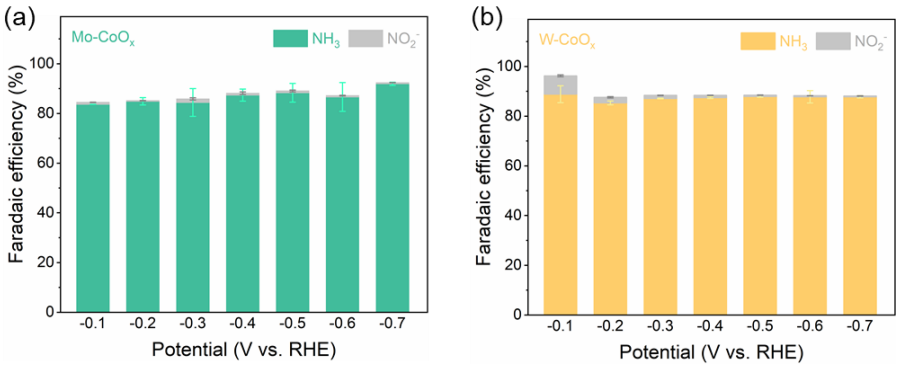

Figure S29. Faradaic efficiency of NH_3 and NO_2^- for the (a) Mo-CoO_x and (b) W-CoO_x electrocatalysts at different potentials.

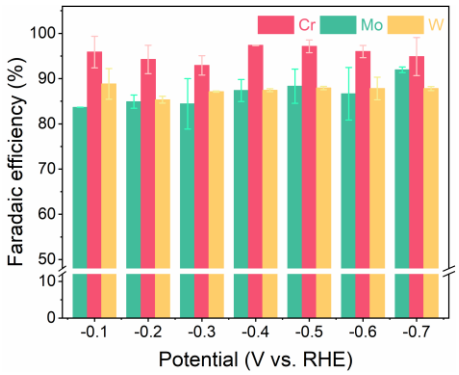

Figure S30. The effect of different doping elements on the Faradaic efficiency of NH_3 at different potentials.

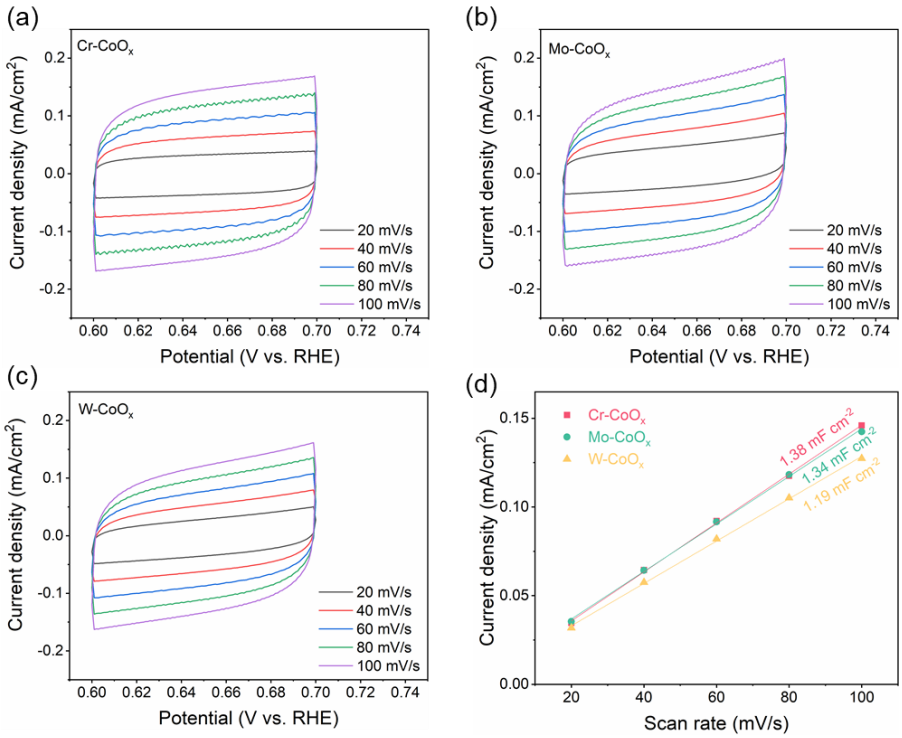

Figure S31. Electrochemically active surface area (ECSA) analysis. Cyclic voltammetry (CV) curves of the (a) Cr-CoO_x, (b) Mo-CoO_x and (c) W-CoO_x catalysts at various scan rates (20 to 100 mV s^{-1}) in the region of 0.6 to 0.7 V vs. RHE. (d) The capacitive current density difference at 0.65 V vs. RHE as a function of scan rates for different electrocatalysts.

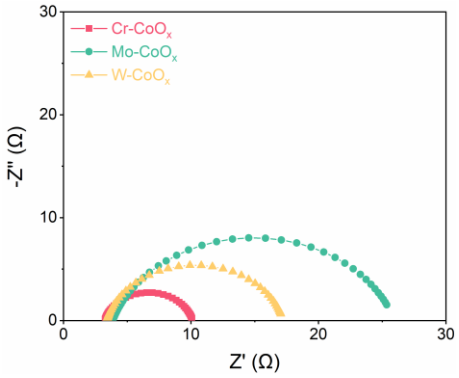

Figure S32. Electrochemical impedance spectra (EIS) of the Cr-CoO_x, Mo-CoO_x and W-CoO_x electrocatalysts.

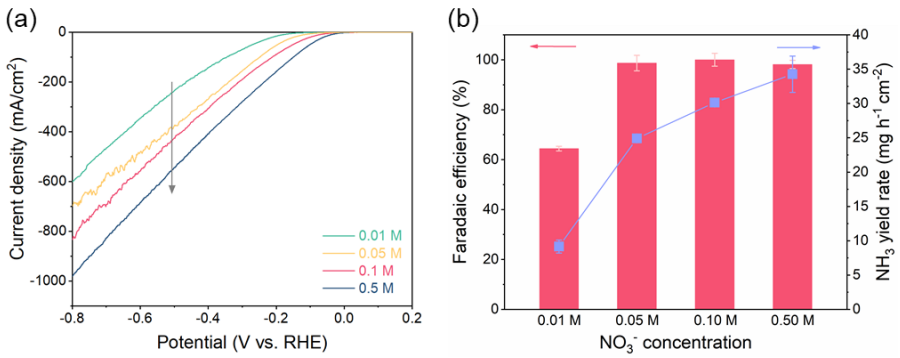

Figure S33. (a) LSV curves of the Cr-CoO_x with different concentration of NO_3^-. (b) NO_3^-RR performance of the Cr-CoO_x with different concentration of NO_3^- at −0.4 V vs. RHE.

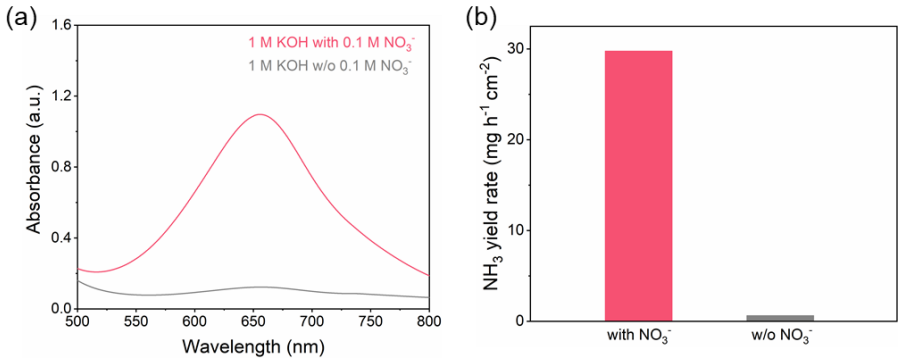

Figure S34. Control experiment results. (a) Spectrophotometric UV-vis curves and (b) NH_3 yield rate of the Cr-CoO_x in 1 M KOH with or without 0.1 M NO_3^- at –0.4 V vs. RHE.

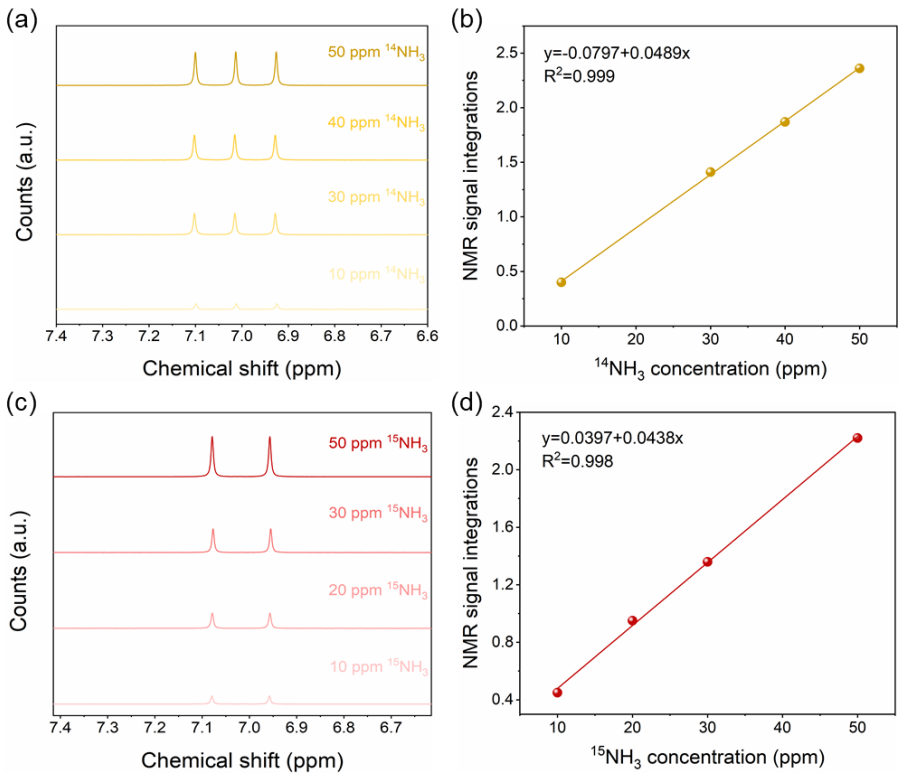

Figure S35. Detection and quantification of $^{15}NH_3$ and $^{14}NH_3$ by ^1H NMR spectra. (a) ^1H NMR spectra of standard $^{14}NH_3$ samples with different concentrations. (b) Calibration curve for $^{14}NH_3$ detection, where $^{14}NH_3$ peak area integrations were normalized to that of maleic acid. (c) ^1H NMR spectra of standard $^{15}NH_3$ samples with different concentrations. (d) Calibration curve for $^{15}NH_3$ detection, where $^{15}NH_3$ peak area integrations were normalized to that of maleic acid.

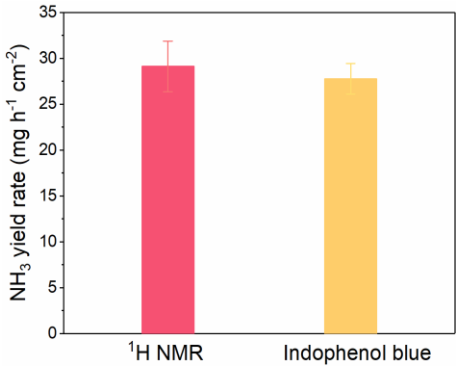

Figure S36. Comparison of the NH_3 yield rate over the Cr-CoO_x electrocatalyst at –0.4 V vs. RHE quantified by the ^{1}H NMR spectra and indophenol blue method.

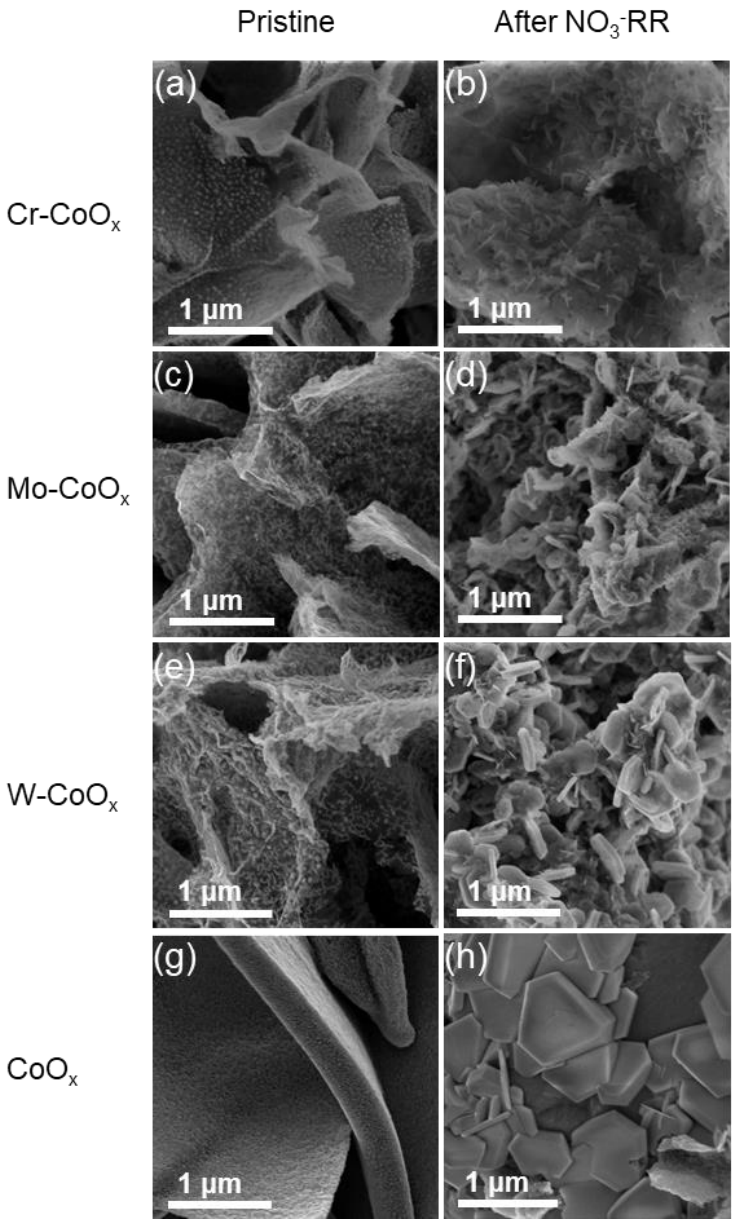

Figure S37. Morphology reconstructions of different electrocatalysts after NO_3^-RR cycling tests. SEM images of (a) the pristine Cr-CoO_x, (b) the Cr-CoO_x after NO_3^-RR tests, (c) the pristine Mo-CoO_x, (d) the Mo-CoO_x after NO_3^-RR tests, (e) the pristine W-CoO_x, (d) the W-CoO_x after NO_3^-RR tests, (e) the pristine CoO_x, (d) the CoO_x after NO_3^-RR tests.

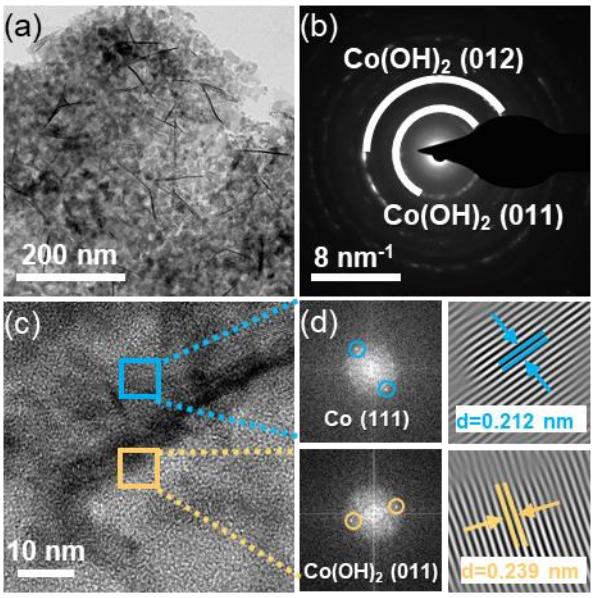

Figure S38. (a) TEM, (b) SAED, (c) HRTEM and (d) corresponding FFT and IFFT images of the Cr-CoO_x after NO_3^-RR cycling tests.

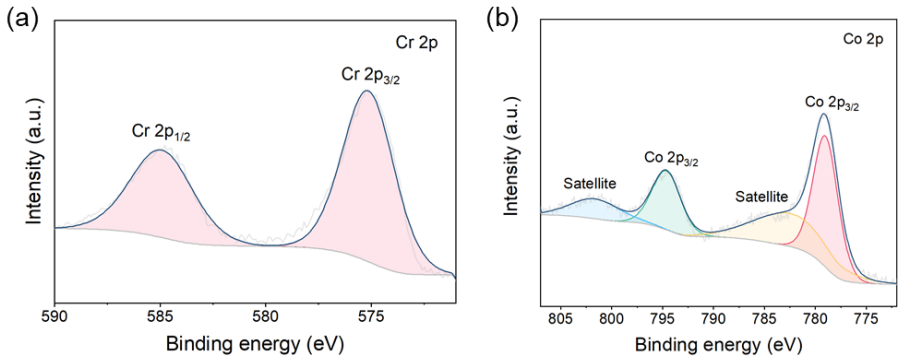

Figure S39. High resolution XPS spectra of (a) Cr 2p and (b) Co 2p of the Cr-CoO_x after NO_3^- RR cycling tests.

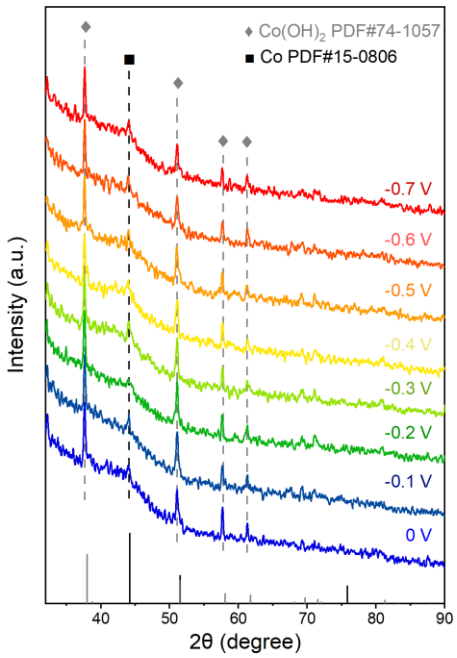

Figure S40. Electrochemical in situ XRD patterns of the Mo-CoO_x.

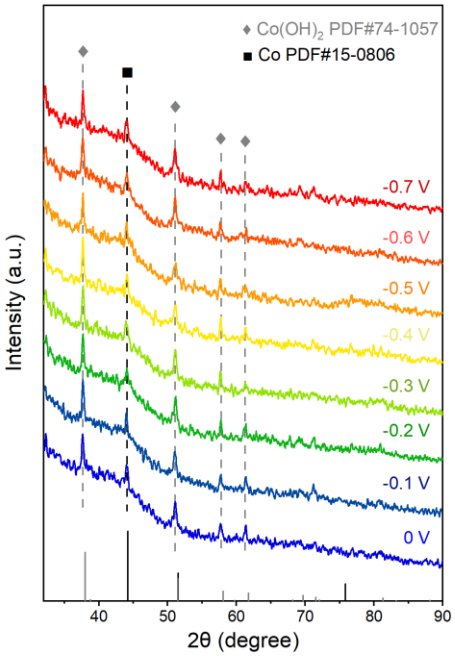

Figure S41. Electrochemical in situ XRD patterns of the W-CoO_x.

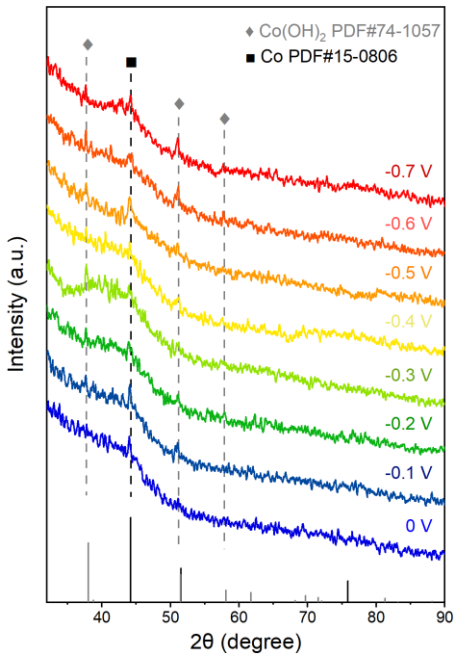

Figure S42. Electrochemical in situ XRD patterns of the CoO_x.

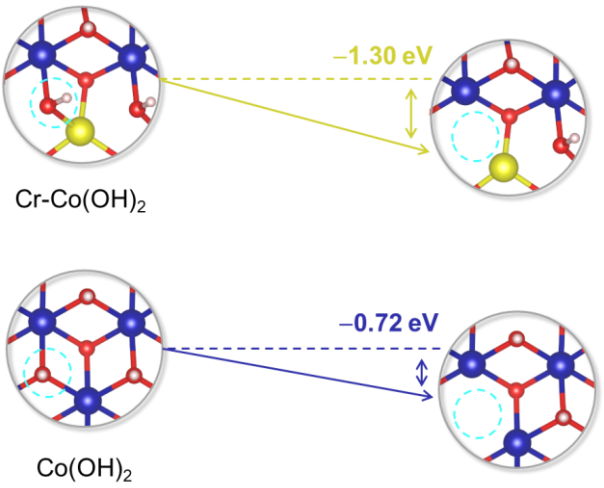

Figure S43. The difference of reconstruction energy between Cr-$Co(OH)_2$ and $Co(OH)_2$.

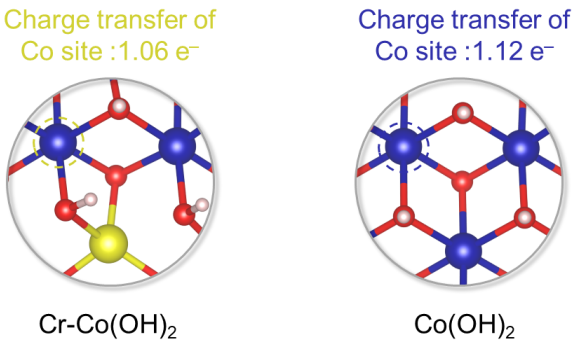

Figure S44. Bader charge analysis of the Co site on Cr-$Co(OH)_2$ and $Co(OH)_2$.

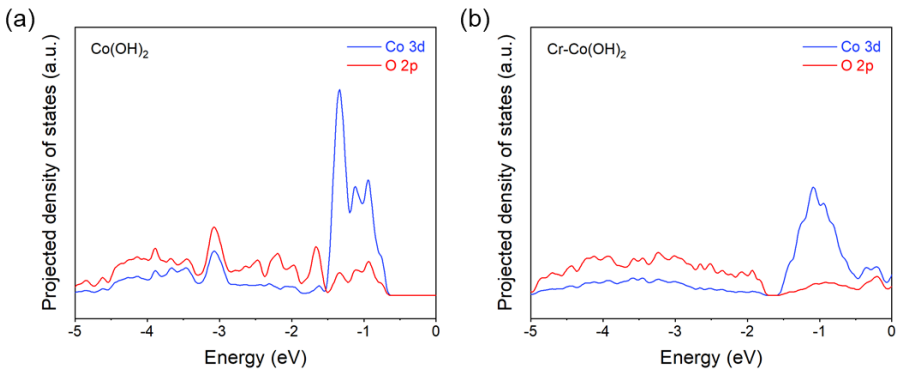

Figure S45. The PDOS calculations for O 2p orbitals and Co 3d orbitals of (a) $Co(OH)_2$ and (b) Cr-$Co(OH)_2$.

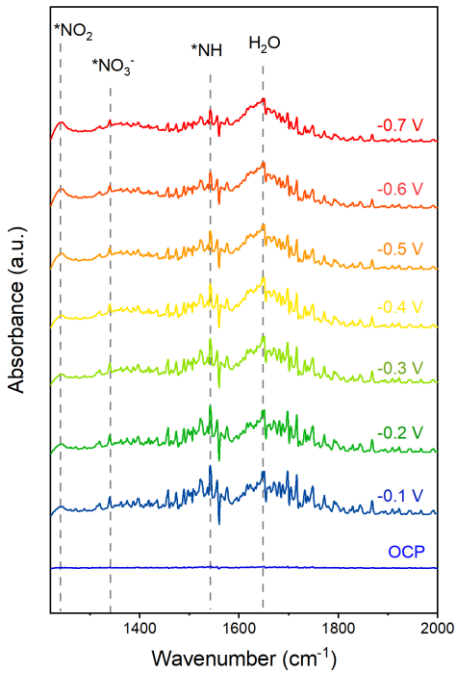

Figure S46. In situ FTIR patterns of the CoO_x.

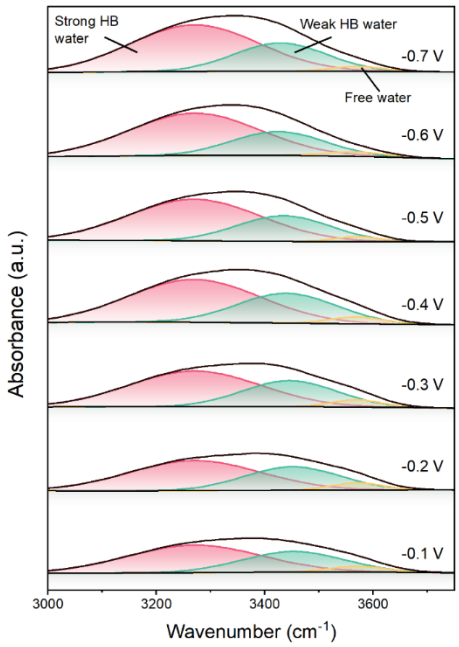

Figure S47. Potential-dependent in situ ATR-FTIR spectra of the O-H stretching mode of interfacial water on the CoO_x electrocatalyst.

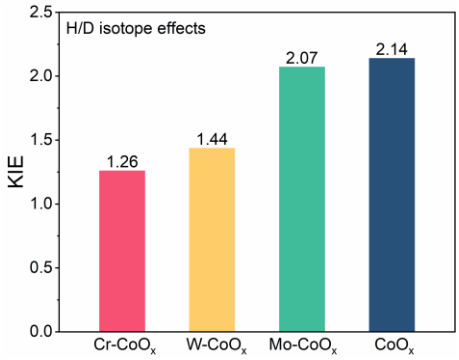

Figure S48. Deuterium kinetic isotope effect (KIE) tests of the Cr-CoO_x, W-CoO_x, Mo-CoO_x and CoO_x electrocatalysts at –0.4 V vs. RHE.

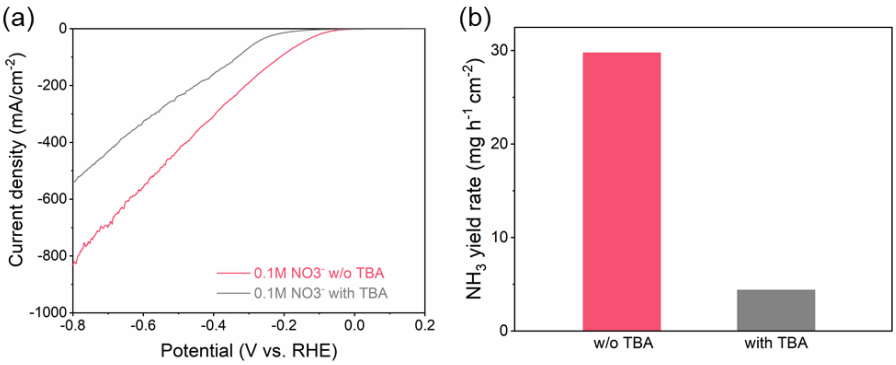

Figure S49. *H quenching experiments. (a) LSV curves and (b) NH_3 yield rate of the Cr-CoO_x in 0.1 M NO_3^- with or without tertiary butanol (TBA) at –0.4 V vs. RHE.

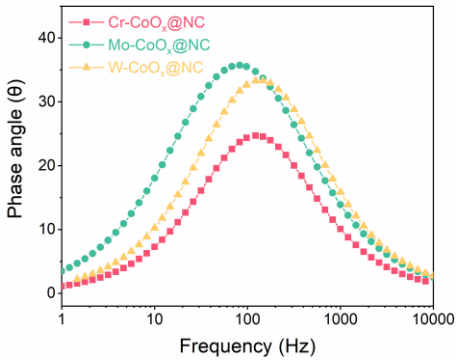

Figure S50. Bode phase plots of the Cr-CoO_x, Mo-CoO_x and W-CoO_x electrocatalysts.

Table S1. Comparison of electrocatalytic NO_3^-RR performance of the Cr-CoO_x electrocatalyst with recently developed electrocatalysts at ambient conditions.

Catalyst	FE (%)	NH_3 yield rate (mg h^{-1} cm^{-2})	Data source
Cr-CoO_x	**97.36**	**58.92**	**This work**
$Ru_{15}Co_{85}$ HNDs	96.8	20.91	*Nat.Catal.*[1]
NiFe-LDH	65.2	0.21	*Nat.Water*[2]
Cu/CuAu SAA	85.5	28.8	*Nat.Synth.*[3]
Ru-CuNW	96	35	*Nat. Nanotechnol.*[4]
$Ni(OH)_x$/Cu	92	51	*Nat.Commun.*[5]
CNS-CoP	90.5	52.58	*Nat.Commun.*[6]
CuCoSP	92.8	2.58	*Nat.Commun.*[7]
L-Cu_xO-HC	95	49.09	*Nat.Commun.*[8]
FePc/TiO_2	90.6	17.4	*Nat.Commun.*[9]
meso-PdN NCs	96.1	3.76	*Adv.Mater.*[10]
$CuCoO_x$ NRs	97.8	3.86	*Adv.Mater.*[11]
Cu/$Co_{0.85}Se_{VSe}$	93.5	2.88	*Adv.Mater.*[12]
RuMo NFs	95.2	6.54	*Adv.Mater.*[13]
CoP/Zn-ZIF	97.2	15.13	*Adv.Mater.*[14]
Cu-RD-KOH	96.5	3.13	*Angew. Chem. Int. Ed.*[15]
Co_3CuN	97	7.74	*Angew. Chem. Int. Ed.*[16]
RuFe-FeNC	92.2	0.012	*Adv. Energy Mater.*[17]
O-$PdFe_3$-mCNFs	96.5	17.23	*Adv. Energy Mater.*[18]
CoP/C@Cu_3P/CF	96.23	28.03	*Energy Environ. Sci.*[19]
Co-B@CoO_x	86.82	0.96	*Energy Environ. Sci.*[20]

References

1 S. Han, H. Li, T. Li, F. Chen, R. Yang, Y. Yu and B. Zhang, *Nat. Catal.*, 2023, **6**, 402-414.

2 K. Wang, R. Mao, R. Liu, J. Zhang, H. Zhao, W. Ran and X. Zhao, *Nat. Water*, 2023, **1**, 1068-1078.

3 Q. Gao, B. Yao, H. S. Pillai, W. Zang, X. Han, Y. Liu, S.-W. Yu, Z. Yan, B. Min, S. Zhang, H. Zhou, L. Ma, H. Xin, Q. He and H. Zhu, *Nat. Synth.*, 2023, **2**, 624-634.

4 F.-Y. Chen, Z.-Y. Wu, S. Gupta, D. J. Rivera, S. V. Lambeets, S. Pecaut, J. Y. T. Kim, P. Zhu, Y. Z. Finfrock, D. M. Meira, G. King, G. Gao, W. Xu, D. A. Cullen, H. Zhou, Y. Han, D. E. Perea, C. L. Muhich and H. Wang, *Nat. Nanotechnol.*, 2022, **17**, 759-767.

5 W. Liu, M. Xia, C. Zhao, B. Chong, J. Chen, H. Li, H. Ou and G. Yang, *Nat. Commun.*, 2024, **15**, 3524.

6 K. Fan, W. Xie, J. Li, Y. Sun, P. Xu, Y. Tang, Z. Li and M. Shao, *Nat. Commun.*, 2022, **13**, 7958.

7 W. He, J. Zhang, S. Dieckhöfer, S. Varhade, A. C. Brix, A. Lielpetere, S. Seisel, J. R. C. Junqueira and W. Schuhmann, *Nat. Commun.*, 2022, **13**, 1129.

8 W. Guo, S. Zhang, J. Zhang, H. Wu, Y. Ma, Y. Song, L. Cheng, L. Chang, G. Li, Y. Liu, G. Wei, L. Gan, M. Zhu, S. Xi, X. Wang, B. I. Yakobson, B. Z. Tang and R. Ye, *Nat. Commun.*, 2023, **14**, 7383.

9 R. Zhang, C. Li, H. Cui, Y. Wang, S. Zhang, P. Li, Y. Hou, Y. Guo, G. Liang, Z. Huang, C. Peng and C. Zhi, *Nat. Commun.*, 2023, **14**, 8036.

10 L. Sun and B. Liu, *Adv. Mater.*, 2023, **35**, 2207305.

11 W. He, S. Chandra, T. Quast, S. Varhade, S. Dieckhöfer, J. R. C. Junqueira, H. Gao, S. Seisel and W. Schuhmann, *Adv. Mater.*, 2023, **35**, 2303050.

12 Z. Gu, Y. Zhang, X. Wei, Z. Duan, Q. Gong and K. Luo, *Adv. Mater.*, 2023, **35**, 2303107.

13 Y. Wang, F. Hao, M. Sun, M.-T. Liu, J. Zhou, Y. Xiong, C. Ye, X. Wang, F. Liu, J. Wang, P. Lu, Y. Ma, J. Yin, H.-C. Chen, Q. Zhang, L. Gu, H. M. Chen, B. Huang and Z. Fan, *Adv. Mater.*, 2024, **36**, 2313548.

14 C. Zhang, Y. Zhang, R. Deng, L. Yuan, Y. Zou, T. Bao, X. Zhang, G. Wei, C. Yu and C. Liu, *Adv. Mater.*, 2024, **36**, 2313844.

15 H. Jiang, G.-F. Chen, O. Savateev, J. Xue, L.-X. Ding, Z. Liang, M. Antonietti and H. Wang, *Angew. Chem. Int. Ed.*, 2023, **62**, e202218717.

16 Z. Gong, X. Xiang, W. Zhong, C. Jia, P. Chen, N. Zhang, S. Zhao, W. Liu, Y. Chen and Z. Lin, *Angew. Chem. Int. Ed.*, 2023, **62**, e202308775.

17 X. Zhao, Y. Jiang, M. Wang, S. Liu, Z. Wang, T. Qian and C. Yan, *Adv. Energy Mater.*, 2023, **13**, 2301409.

18 M. Xie, G. Zhu, H. Yang, B. Liu, M. Li, C. Qi, L. Wang, W. Jiang, P. Qiu and W. Luo, *Adv. Energy Mater.*, 2024, **14**, 2401717.

19 Y. Li, Z. Lu, L. Zheng, X. Yan, J. Xie, Z. Yu, S. Zhang, F. Jiang and H. Chen, *Energy Environ. Sci.*, 2024, **17**, 4582-4593.

20 X. Zhu, C. Ma, Y.-C. Wang, K. Qu, L. Song, J. Wang, Y. Gong, X. Liu, J. Zhang, Q. Lu and A.-L. Wang, *Energy Environ. Sci.*, 2024, **17**, 2908-2920.